Analytical model of the source and radiation of sound from the trailing edge of a swept airfoil

G. Grasso, M. Roger, S. Moreau

Analytical model of the source and radiation of sound from the trailing edge of a swept airfoil

G. Grasso[a,*], M. Roger[a], S. Moreau[b]

[a] *Univ Lyon, École Centrale de Lyon, INSA Lyon, Université Claude Bernard Lyon I, CNRS, Laboratoire de Mécanique des Fluides et d'Acoustique, UMR 5509, 36 Avenue Guy de Collongue, F-69134, Écully, France*
[b] *Département de Génie Mécanique, Université de Sherbrooke, Sherbrooke, QC, J1K 2R1, Canada*

Abstract

Highly-swept blades are used in automotive cooling systems, in the fans of modern ultra-high by-pass ratio engines and in counter-rotating open rotors, in part in order to reduce noise emission. The present work investigates the effect of sweep on the free-field noise emission from the trailing edge of an isolated airfoil analytically, as a first step towards a more complete approach dedicated to rotating blades. Firstly, Amiet-Schwarzschild's technique is extended to the case of a swept airfoil in order to assess the effect of sweep on the sound directivity both by a single three-dimensional gust and by the combined effect of all gusts at a given frequency. It is found that sweep produces a non-symmetric directivity pattern, similar to the effect of a skewed gust. Sweep also affects the wavenumber distribution of the wall-pressure fluctuations beneath a turbulent boundary layer. This effect is studied by means of a generalised Corcos' model, which allows distributing energy in the chordwise and spanwise wavenumber ranges independently. The role of the spanwise-wavenumber distribution of wall-pressure power spectral density in amplifying the radiated noise is investigated and shown to have a limited impact.

Keywords: Airfoil trailing-edge noise, Free-field sound propagation, Wall-pressure fluctuations model

Nomenclature

b	airfoil half-chord
c	airfol chord measured in the flow direction
c_0	speed of sound

*Corresponding author. Currently affiliated with Cenaero France, 42 rue de l'Innovation, 77550 Moissy-Cramayel, France.
Email address: gabriele.grasso@cenaero.fr (G. Grasso)

k	ω/c_0, acoustic wavenumber
k_x, k_y	aerodynamic wavenumbers relative to a rectangular airfoil
k'_x, k'_y	aerodynamic wavenumbers relative to a swept airfoil
$\mathbf{K}$	wavenumber vector
$\mathcal{L}^{\text{sup}}, \mathcal{L}^{\text{sub}}$	aeroacoustic transfer functions for supercritical and subcritical gusts, respectively
l_y	spanwise correlation length of wall-pressure fluctuations
M_i	U_i/c_0, Mach number based on i-th mean velocity component
p', p, P	fluctuating pressure variables
R_T	ratio of timescales of pressure
S_{pp}	far-field acoustic power spectral density
sinc	sine cardinal function
$\mathbf{x} = x_1, x_2, x_3$	observer position in a coordinate system centered on the trailing edge of an airfoil
U_c	convective speed of wall-pressure fluctuations
U_0	mean flow speed
U_x	projection of mean flow speed on x' axis
U_y	projection of mean flow speed on y' axis
α	U_0/U_c
β_i	$\sqrt{1-M_i^2}$, compressibility factor based on i-th mean velocity component
β_C	Clauser's parameter
γ	gust oblique angle
δ	boundary layer thickness
δ^*	boundary layer displacement thickness
Δ	δ/δ^*
η_x, η_y	distance between two points on the airfoil surface in the x and y directions, respectively
Π	wake strength parameter
$\Pi(\omega, k_x, k_y)$	two-wavenumber-frequency spectral density of wall-pressure fluctuations
$\Pi_0(\omega, k_y)$	one-wavenumber-frequency spectral density of wall-pressure fluctuations
ρ_0	flow density in a quiescent medium
$\tau_{\max}$	maximum shear stress across the boundary layer
$\varphi_{pp}(\omega)$	single-point frequency spectrum of wall-pressure fluctuations
ψ	sweep angle
ω	reduced frequency
$\overline{(\cdot)}$	normalization by the half-chord, b
$(\cdot)^*$	complex conjugate

1. Introduction

The turbulent boundary layer over an aerodynamic profile generates a spectrum of wall-pressure fluctuations that is scattered as acoustic waves at the trailing edge. In general, this broadband trailing-edge noise is the minimum achievable noise of a blade operating in a homogeneous stationary flow. It is therefore of great interest in a variety of industrial applications, typically low-Mach number cooling fans but also ultra-high by-pass ratio (UHBR) engines and counter-rotating open rotors (CROR). In particular, these aero-engine architectures both allow for a substantial reduction of fuel consumption. Ongoing

research also focuses on the mechanisms of their noise emission to further reduce the environmental impact of air transportation. For car-engine cooling fans, noise reduction achieved with sweep is a possible way of improving passenger comfort.

It is worth noting that the definitions of sweep and lean may vary according to the industrial context. In low-speed axial-flow turbomachines, sweep refers to the azimuthal displacement of blade cross-sections, either forward or backward with respect to the direction of rotation, by opposition to a radial (unswept) blade stacking. In this case, shifting the cross-sections axially is referred to as lean. They have both aerodynamic and acoustic effects. In the case of high-speed turbomachines, the opposite convention applies: sweep denotes blade stacking in the axial or flow direction, whereas lean is in the circumferential or flow-normal direction. In the present paper dealing with isolated airfoils, sweep is defined as the angle of the relative flow with respect to the normal to the trailing-edge. In that general sense, it can be retained as a generic definition including blade skewness. The use of swept blades for the mitigation of several noise generation mechanisms in aeroengine architectures and low-speed ventilation systems has been investigated experimentally and numerically over the years. Vad [1] studied different leading- and/or trailing-edge swept airfoil configurations and concluded that local unloading of the airfoil can be achieved by applying sweep to either edge, irrespectively of the shape of the stacking line, because only the component of the mean velocity perpendicular to the edge contributes to lift generation. Envia *et al.* [2, 3] investigated the effect of swept and leaned rotor blades and stator vanes in turbofans. De Laborderie and Moreau [4] presented a model of the sound transmitted in a duct from a three dimensional row of outlet guide vanes due to wake interaction. They performed a parametric study of the combined effect of sweep and lean. They concluded that lean was more effective than sweep and that a combined effect could yield an even larger noise mitigation. Woodward *et al.* [5] found experimentally that swept vanes significantly reduce the tonal interaction noise emitted by a turbofan. The common conclusion of these studies is that sweep increases the phase changes from hub to tip of the unsteady aerodynamics producing noise thus reducing the source strength (see also [6]). Grasso *et al.* [7] introduced sweep as a design variable in the AI-driven design of a counter-rotating fan in order to make the most of this effect. Casalino *et al.* [8] investigated the effect of serrations on swept OGVs, finding that the interaction noise could only be marginally further reduced if the characteristic dimensions of the serrations are sufficiently large compared to the integral scales of the impinging turbulent fluctuations. The role of sweep in the reduction of noise from low-speed axial fans may be more complicated to assess than in the case of turbofans. For instance, in the optimization of a swept benchmark fan carried out by Bamberger & Carolus [9] it was not clear whether the noise reduction was due to sweep or to the reduction of secondary flows. The influence of the operating conditions of the fan on the possibility of reducing noise by means of sweep is highlighted in [10], [11] and [12]. Herold *et al.* [10] also pointed out that vortex shedding from the trailing-edge of a blade is significantly dependent on the component

of the mean flow speed perpendicular to the edge. Therefore, sweep could help reducing this noise generation mechanism as well. The main motivation of the present work is to assess an analytical model as a possible way of quantifying the benefit of sweep, usable at the early design stage.

Amiet-Schwarzschild's approach [13, 14] is selected. It calculates trailing-edge noise from a consistent model of boundary-layer turbulence, with stationary statistical properties, convecting past a trailing edge. The theory was originally developed for the case of an airfoil with unswept trailing edge. Likewise, Amiet's model of leading-edge turbulence interaction noise [15] was originally formulated considering an unswept leading edge. It has been later extended to the investigation of the effect of sweep. This feature was first introduced in the analytical formulation of Amiet's leading-edge theory by Rozenberg [16], followed by Carazo *et al.* [17, 18] who studied the effect of sweep in CROR wake-interaction noise. The same approach was applied to the study of blade-vortex impingement noise by Roger *et al.* [19] and Quaglia *et al.* [20]. The expression of the unsteady lift generated on the swept airfoil by any Fourier component of the hydrodynamic disturbance was found identical to results obtained by Adamczyk [21] using the Wiener-Hopf technique.

Concerning the trailing-edge noise modeling, the main scattering formulation obtained by Amiet [22] has been corrected by taking into account a leading-edge back-scattering contribution with a second application of Schwarzschild's technique [23, 24], in order to improve the low-frequency prediction. However, this theory again refers only to the case of an edge perpendicular to the mean flow velocity. The aim of the present paper is to introduce the sweep angle in Amiet's formulation of trailing-edge noise. It will be shown that this modification of the original formulation has a twofold effect. On the one hand, sweep modifies the directivity of the noise emitted at a given frequency with respect to the case of a rectangular airfoil, all other conditions being held constant, as was already noticed in the corresponding leading-edge study [17]. On the other hand, the distribution of energy of the incident wall-pressure field is also modified due to the rotation of the reference frame aligned with the edge. It is interesting to investigate this effect as well, because the power spectral density (PSD) of the acoustic pressure is directly proportional to that of the incident wall-pressure fluctuations. Therefore the quantification of wall-pressure statistics is critical for obtaining an accurate sound prediction.

Various models of the spectrum of wall-pressure fluctuations are available in the literature, which are either semi-empirical or based on the Poisson equation governing the unsteady pressure in an incompressible turbulent boundary layer (see [25] and [26] for exhaustive reviews of either category). Sound predictions obtained with Amiet's theory are very sensitive to the selected wall-pressure spectrum formulation, as shown in [27, 28]. For this reason, the calculations presented in this work are carried out using a model of the statistics of the wall-pressure fluctuations in the wavenumber domain that can be adjusted, in order to evaluate the effect of different wavenumber-domain distributions on the emitted noise.

Finally, the sound propagation theory developed in Section 2 is linked in

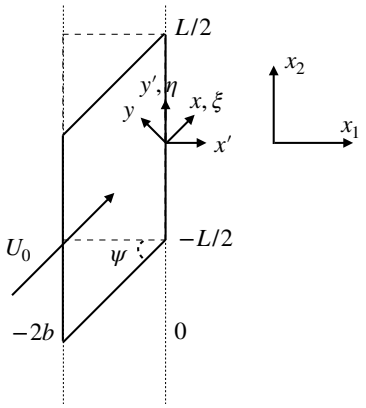

Figure 1: Reference frames and integration surfaces considered for the formulation of the noise radiated by a swept blade segment (adapted from [17]).

Section 5 to the strip-theory approach used in rotating machinery noise prediction.

2. Application of Amiet-Schwarzschild's method to the noise emitted by a swept trailing-edge

2.1. Derivation of the canonical wave equation for the disturbance pressure

An analytical expression is sought for the disturbance pressure generated as an incident wall-pressure field is convected past the trailing edge of an airfoil. The disturbance pressure acts as equivalent acoustic sources and the corresponding far-field sound pressure is obtained from Curle's acoustic analogy, yielding a closed-form expression of the aeroacoustic transfer function. The trailing edge is first assimilated to the edge of a half-plane for the application of Schwarzschild's theorem. The correction for back-scattering from the leading edge is obtained with a second iteration of Schwarzschild's technique, which takes the solution of the first iteration as input. It has been shown in [24] that the effect of the back-scattering correction is significant mainly at low frequencies.

The analytical developments presented below follow those of Roger & Moreau [23] for the case of an unswept airfoil as in Fig. 1 (dashed lines). If the sweep angle, ψ, defined in Fig. 1 vanishes, the following results coincide with those of [23].

The convected wave equation for the disturbance pressure is written as

$$\nabla^2 p' - \frac{1}{c_0^2}\frac{\mathrm{D}^2}{\mathrm{D}t^2}p' = 0. \tag{1}$$

Due to the introduction of sweep, the mean flow speed has a finite component along the span of the airfoil and therefore the total derivative operator has the

form

$$\frac{\mathrm{D}}{\mathrm{D}t} = \frac{\partial}{\partial t} + U_x \frac{\partial}{\partial x'} + U_y \frac{\partial}{\partial y'}. \tag{2}$$

Sinusoidal pressure gusts are defined by wavenumbers (k_x, k_y) in the reference frame aligned with the mean flow, (x, y), which are transposed in the frame attached to the swept airfoil trailing-edge, (x', y'), with the following transformation:

$$\begin{cases} k'_x = k_x \cos\psi - k_y \sin\psi \\ k'_y = k_x \sin\psi + k_y \cos\psi. \end{cases} \tag{3}$$

Factorising the disturbance pressure at the reduced frequency ω as

$$\begin{aligned} p'(x', y', z, t) &= P(x', y', z)\mathrm{e}^{\mathrm{i}\omega t} \\ P(x', y', z) &= p(x', z)\mathrm{e}^{\mathrm{i}(k'_x M_x^2/\beta_x^2)x'}\,\mathrm{e}^{-\mathrm{i}k'_y y'} \end{aligned}$$

and using Prandtl-Glauert/Reissner/Lorentz transformation allows re-writing Eq. (1) as a canonical wave equation

$$\frac{\partial^2 p}{\partial X'^2} + \frac{\partial^2 p}{\partial Z^2} + \kappa^2 p = 0 \tag{4}$$

with the normalized coordinates $X' = x'/b$, $Y' = y'\beta_x/b$ and $Z = z\beta_x/b$ and the parameter

$$\kappa^2 = \mu^2 - \frac{\overline{k}_y'^2}{\beta_x^2} \qquad \text{with} \qquad \mu^2 = \frac{\overline{k}_x'^2 M_x^2}{\beta_x^4}. \tag{5}$$

If $\kappa^2 > 0$, the differential equation is hyperbolic and the gust is said supercritical, whereas if $\kappa^2 < 0$, the differential equation is elliptic and the gust is said subcritical. Subcritical gusts induce evanescent pressure waves in the case of an infinite-span airfoil. However, they are considered because the acoustic field is obtained by integrating the effect of all gusts over the actual - finite - airfoil surface, in which case they were shown to contribute significantly at low frequencies [23].

2.2. Solution of the canonical wave equation

2.2.1. Main trailing-edge contribution

An incident-pressure sinusoidal gust of unitary amplitude and frequency ω, convected towards the trailing edge with speed $U_c = U_0/\alpha$, with $\alpha > 1$, can be represented as

$$\begin{aligned} p'_0(x', y', z, t) &= \mathrm{e}^{-\mathrm{i}\alpha k'_x x'}\,\mathrm{e}^{\mathrm{i}\omega t} \\ P_0(x', y', z) &= \mathrm{e}^{-\mathrm{i}k'_x x'(\alpha + M_x^2/\beta_x^2)}\mathrm{e}^{\mathrm{i}k'_y y'/\beta_x}. \end{aligned}$$

The convection speed U_c is assumed parallel to the mean flow speed, U_0. It is worth noting that arbitrary inclination of the convection speed of the boundary-layer turbulence with respect to the trailing edge has been addressed by Howe

in a review paper on trailing-edge noise theories [29]. Yet the author considered an external flow normal to the edge. This mixed assumption is *a priori* relevant in the case of blades for which a radial fluid motion occurs. The formulation presented in this work, assuming that both the convection speed and the free-stream velocity are parallel, is compatible with the radial-equilibrium condition. The other difference with Howe's analysis is that a finite chord length is explicitly taken into account.

It is also assumed that the wall is perfectly rigid. Therefore the normal-to-wall gradient of the corresponding disturbance pressure, p_1', vanishes on the half-plane. Furthermore the disturbance pressure is equal and opposite to the incident pressure field at the trailing edge and in the wake according to the Kutta condition. These boundary conditions are expressed as

$$\begin{cases} \dfrac{\partial p_1}{\partial Z}(X',0) = 0 & \text{for} \quad X' < 0 \\ p_1(X',0) = -\mathrm{e}^{-\mathrm{i}\overline{k}_x' X'(\alpha + M_x^2/\beta_x^2)} \mathrm{e}^{\mathrm{i}\overline{k}_y' Y'/\beta_x} & \text{for} \quad X' \geq 0. \end{cases} \tag{6}$$

Schwarzschild's theorem [14] provides the following solution of the canonical equation (4) for the disturbance pressure with the boundary conditions of Eq. (6) for $X' < 0$:

$$p_1(X',0) = -\frac{1}{\pi} \mathrm{e}^{\mathrm{i}\overline{k}_y' Y'/\beta_x} \int_0^\infty \sqrt{-\frac{X'}{\zeta}} \frac{\mathrm{e}^{-\mathrm{i}\kappa(\zeta - X')}}{\zeta - X'} \mathrm{e}^{-\mathrm{i}\overline{k}_x' \zeta(\alpha + M_x^2/\beta_x^2)} \mathrm{d}\zeta. \tag{7}$$

Defining the complex-valued function

$$E^*(x) = \int_0^x \frac{\mathrm{e}^{-\mathrm{i}t}}{\sqrt{2\pi t}} \mathrm{d}t = C_2(x) - \mathrm{i}S_2(x)$$

where C_2 and S_2 are the Fresnel integrals (see [30]), Eq. (7) is re-formulated in the supercritical case ($\kappa > 0$) as

$$P_1^{\mathrm{sup}}(X',0) = \mathrm{e}^{-\mathrm{i}\alpha\overline{k}_x' X'} \left[(1+i) E^* \left(-(\alpha\overline{k}_x' + \kappa + \mu M_x) X' \right) - 1 \right]. \tag{8}$$

If $\psi = 0$ and $k_y' = 0$, this corresponds to the original result derived by Amiet in [22].

Equation (7) is applied to the subcritical case ($\kappa^2 < 0$) as well by defining the parameter

$$\kappa'^2 = -\kappa^2 = \frac{\overline{k}_y'^2}{\beta_x^2} - \mu^2.$$

Although κ' is a double-valued constant ($\kappa' = \pm\mathrm{i}\kappa$), it is necessary to select the proper branch cut $\kappa' = -\mathrm{i}\kappa$ to ensure the asymptotic decay to zero at an infinite distance from the source of the scattered pressure field. Defining the complex error function $\Phi^0(\sqrt{\mathrm{i}x}) = \sqrt{2}\mathrm{e}^{\mathrm{i}\pi/4} E^*(x)$, the subcritical disturbance pressure solution is expressed as

$$P_1^{\mathrm{sub}}(X',0) = \mathrm{e}^{-\mathrm{i}\alpha\overline{k}_x' X'} \left[\Phi^0 \left(\left[-i(\alpha\overline{k}_x' - \mathrm{i}\kappa' + \mu M_x) X' \right]^{1/2} \right) - 1 \right]. \tag{9}$$

2.2.2. Leading-edge back-scattering correction

The main trailing-edge disturbance pressure derived in the previous section can be corrected by adding a term that accounts for the back-scattering from the leading edge. The problem is expressed in terms of the disturbance potential, Φ, which is related to the disturbance pressure by the equation

$$P\mathrm{e}^{\mathrm{i}\omega t} = -\rho_0 \frac{D\Phi}{Dt} \tag{10}$$

with $\Phi = \phi\, \mathrm{e}^{\mathrm{i}\omega t}$. Applying Eq. (2), the previous equation becomes

$$-\frac{b}{\rho_0 U_x} P = \mathrm{i}\overline{k}'_x \phi + \frac{\partial \phi}{\partial X'}. \tag{11}$$

Therefore, the trailing-edge disturbance potential is

$$\phi_1(X',0) = -\frac{b}{\rho_0 U_x} \int_{-\infty}^{X'} P_1(\zeta,0) \mathrm{e}^{-\mathrm{i}\overline{k}'_x(\zeta - X')} \mathrm{d}\zeta. \tag{12}$$

The variable transformation

$$\psi_1 = \phi_1\, \mathrm{e}^{\mathrm{i}\overline{\mu} M X'}, \quad \nu = -(X' + 2)$$

allows formulating a Schwarzschild's problem analogous to that of Eq. (4) with the following boundary conditions:

$$\begin{cases} \psi_2(\nu,0) = -\psi_1(\nu,0) \quad \text{for } \nu > 0, \\ \frac{\partial \psi_2}{\partial Z}(\nu,0) = 0 \quad \text{for } \nu \leq 0. \end{cases} \tag{13}$$

The first condition cancels the trailing-edge disturbance potential upstream of the leading edge ($X' < -2$), whereas the second condition represents a perfectly rigid wall extending infinitely downstream of the leading edge ($X' \geq -2$). As a consequence, the leading-edge correction potential, ψ_2, does not fulfill the Kutta condition and should be corrected with a third trailing-edge back-scattering term. Further iterations of the Schwarzschild technique, however, are not necessary as shown in [15]. In particular, it has been demonstrated in [24] that the leading-edge back-scattering contribution to the overall radiated noise tends to vanish at high frequencies.

The solution to the leading-edge Schwarzschild's problem is

$$\psi_2(\nu,0) = -\frac{1}{\pi} \int_0^{\infty} \sqrt{\frac{-\nu}{\zeta}} \frac{\mathrm{e}^{-\mathrm{i}\kappa(\zeta - \nu)}}{\zeta - \nu} \psi_1(\nu,0) \mathrm{d}\zeta.$$

This integral, unfortunately, has no closed-form analytical solution. However, it is shown in [23], that a reasonable approximation of the back-scattering disturbance pressure is given- for a supercritical incident gust- by

$$\begin{aligned} P_2^{\mathrm{sup}}(X',0) \simeq & \frac{(1+\mathrm{i})\mathrm{e}^{-4\mathrm{i}\overline{\kappa}}}{2\sqrt{\pi}(\alpha - 1)\overline{k}'_x} \frac{1 - \Theta_1^2}{\sqrt{A_1}} \mathrm{e}^{\mathrm{i}(M_x\overline{\mu} - \overline{\kappa})X'} \\ & \times \left[\mathrm{i}\left\{ \overline{k}'_x + M_x\overline{\mu} - \overline{\kappa} \right\} \{F(X')\}^c + \left\{ \frac{\partial F(X')}{\partial X'} \right\}^c \right] \end{aligned} \tag{14}$$

with the parameters

$$A_1 = \alpha\overline{k}_x' + M_x\overline{\mu} + \overline{\kappa}, \quad A = \overline{k}_x' + M_x\overline{\mu} + \overline{\kappa}, \quad \Theta_1 = \sqrt{\frac{A_1}{A}} \tag{15}$$

and the function

$$F(X') = \mathrm{e}^{2\mathrm{i}\overline{\kappa}(X'+2)}\left\{1 - (1+\mathrm{i})E^*\left[2\overline{\kappa}(X'+2)\right]\right\}. \tag{16}$$

The superscript $\{-\}^c$ represents the multiplication of the imaginary part of the argument by the correction factor $\varepsilon = \left(1 + \frac{1}{4\overline{\mu}}\right)^{-1/2}$. This correction is needed to match the approximate analytical solution of Schwarzschild's integral with its numerical computation. Finally, the leading-edge back-scattering disturbance pressure generated by a subcritical incident gust is

$$\begin{aligned} P_2^{\mathrm{sub}}(X',0) \simeq & \frac{(1+\mathrm{i})(1-\Theta_1'^2)}{2\sqrt{\pi}(\alpha-1)\overline{k}_x'\sqrt{A_1'}}\mathrm{e}^{\mathrm{i}(M_x\overline{\mu}-\mathrm{i}\overline{\kappa'})X'} \\ & \times\left[\mathrm{i}\left\{\overline{k}_x' + M_x\overline{\mu} - \mathrm{i}\overline{\kappa'}\right\}F'(X') + \frac{\partial F'(X')}{\partial X'}\right] \end{aligned} \tag{17}$$

with the parameters

$$A_1' = \alpha\overline{k}_x' + M_x\overline{\mu} - \mathrm{i}\overline{\kappa'}, \quad A' = \overline{k}_x' + M_x\overline{\mu} - \mathrm{i}\overline{\kappa'}, \quad \Theta_1' = \sqrt{\frac{A_1'}{A'}} \tag{18}$$

and the function

$$F'(X') = 1 - \mathrm{erf}\left(\sqrt{2\overline{\kappa'}(X'+2)}\right). \tag{19}$$

In this case, the correction of the imaginary part is not needed.

2.3. Expression of the far-field acoustic pressure

The acoustic far-field pressure corresponding to a disturbance pressure harmonic of unit amplitude and wavenumber $\mathbf{K} = (k_x', k_y')$ is calculated by means of Curle's analogy [31] as

$$p_K(\mathbf{x},\omega) = -\frac{\mathrm{i}\omega\, x_3}{4\pi c_0 S_0^2}\int_{S_y}\Delta P(X',0)\mathrm{e}^{\mathrm{i}\omega R_t/c_0}\mathrm{e}^{-\mathrm{i}\overline{k}_y' Y'}\,\mathrm{d}S_y \tag{20}$$

where $\Delta P = 2P = 2(P_1 + P_2)$ is the induced source distribution accounting for the opposite disturbance pressures induced on both sides of the airfoil, acting as an equivalent dipole distribution. The convection of acoustic waves by an external mean flow with velocity components U_x and U_y along the x' and y' directions, respectively, is accounted for using the following modified coordinates (see [16]):

$$R_t = \frac{1}{\beta_0^2}\left(R_s - M_x(x_1 - x') - M_y(x_2 - y')\right),$$

$$R_s \approx S_0 \left(1 - \frac{(1-M_y^2)x_1x' + (1-M_x^2)x_2y'}{S_0^2}\right)$$

and

$$S_0 = \sqrt{{\beta_y}^2 x_1^2 + {\beta_x}^2 x_2^2 + \beta_0^2 x_3^2}.$$

Equation (20) contains a double integral of the equivalent dipole distribution over the airfoil surface. Considering the parallelogram shape of the swept airfoil, this integral is solved in the non-Cartesian reference frame (ξ, η) represented in Fig. 1, such that

$$\begin{cases} x' = \xi \cos\psi \\ y' = \eta + \xi \sin\psi. \end{cases} \tag{21}$$

Introducing the coordinate transformation of Eq. (21) in Eq. (20) yields the following expression of the integral:

$$p_K(\mathbf{x},\omega) = -\frac{\mathrm{i}\omega\, x_3 \cos\psi}{2\pi c_0 S_0^2} b^2 \int_{-\frac{2}{\cos\psi}}^{0} \int_{-\frac{L}{2b}}^{\frac{L}{2b}} P\left(\overline{\xi}, 0\right) \mathrm{e}^{\mathrm{i}\omega R_t/c_0} \mathrm{e}^{-\mathrm{i}\overline{k}'_y(\overline{\eta} + \overline{\xi}\sin\psi)} \mathrm{d}\overline{\xi}\mathrm{d}\overline{\eta}. \tag{22}$$

The complex amplitude of the source distribution $f(X')$ can be defined such as $P = f(X')\mathrm{e}^{-\mathrm{i}\left(\overline{k}'_x X' + \overline{k}'_y Y'\right)}$; furthermore, defining the parameter

$$C = \alpha\overline{k}'_x + \overline{k}'_y \tan\psi - \frac{\overline{k}}{\cos\psi\, \beta_0^2}\left(\frac{\beta_y^2 x_1 \cos\psi}{S_0} + \frac{\beta_x^2 x_2 \sin\psi}{S_0} - M_0\right), \tag{23}$$

the double integral appearing in Eq. (22) can be separated in its two variables:

$$\begin{aligned} p_K(\mathbf{x},\omega) = &-\frac{\mathrm{i}\omega\, x_3 \cos\psi}{2\pi c_0 S_0^2} b^2 \mathrm{e}^{\mathrm{i}k/\beta_0^2(S_0 - M_x x_1 - M_y x_2)} \int_{-\frac{2}{\cos\psi}}^{0} f\left(\overline{\xi}\right) \mathrm{e}^{-\mathrm{i}C\overline{\xi}\cos\psi} \mathrm{d}\overline{\xi} \\ &\times \int_{-\frac{L}{2b}}^{\frac{L}{2b}} \mathrm{e}^{-\mathrm{i}\overline{\eta}\left[\overline{k}'_y - \overline{k}/\beta_0^2(\beta_x^2 x_2/S_0 - M_y)\right]} \mathrm{d}\overline{\eta}. \end{aligned} \tag{24}$$

Consequently, the integral involving $\overline{\eta}$ is independent of the dipole distribution and can be solved as

$$b\int_{-\frac{L}{2b}}^{\frac{L}{2b}} \mathrm{e}^{-\mathrm{i}\overline{\eta}\left[\overline{k}'_y - \overline{k}/\beta_0^2(\beta_x^2 x_2/S_0 - M_y)\right]} \mathrm{d}\overline{\eta} = L\ \mathrm{sinc}\left(\frac{L}{2b}\left[\overline{k}'_y - \frac{\overline{k}}{\beta_0^2}\left(\frac{\beta_x^2 x_2}{S_0} - M_y\right)\right]\right). \tag{25}$$

The integral involving $\overline{\xi}$ represents the aeroacoustic transfer function, $\mathcal{L}$, which is the sum of the main trailing-edge contribution and of the leading-edge back-scattering correction: $\mathcal{L} = \mathcal{L}_1 + \mathcal{L}_2$. Thus, the far-field acoustic pressure at a point $\mathbf{x}$ and a frequency ω, generated by a disturbance pressure gust of unit amplitude and wavenumber $\mathbf{K}$, is

$$\begin{aligned} p_K(\mathbf{x},\omega) = &-\frac{\mathrm{i}\omega\, x_3\, Lb\, \cos\psi}{2\pi c_0 S_0^2} \mathrm{e}^{\mathrm{i}k/\beta_0^2(S_0 - M_x x_1 - M_y x_2)} \\ &\times \mathrm{sinc}\left(\frac{L}{2b}\left[\overline{k}'_y - \frac{\overline{k}}{\beta_0^2}\left(\frac{\beta_x^2 x_2}{S_0} - M_y\right)\right]\right)\mathcal{L}. \end{aligned} \tag{26}$$

2.3.1. Main trailing-edge aeroacoustic transfer function

It is possible to derive an analytical expression of the aeroacoustic transfer function, $\mathcal{L}$. In order to derive the main trailing-edge term in the supercritical case, we define the complex amplitude of the source distribution

$$f_1^{\mathrm{sup}}\left(\overline{\xi}\right) = (1+\mathrm{i})E^*\left[-B\overline{\xi}\cos\psi\right] - 1$$

with the parameter

$$B = \alpha\overline{k}'_x + \mu\, M_x + \kappa.$$

Consequently,

$$\begin{aligned}\mathcal{L}_1^{\mathrm{sup}}(k'_x, k'_y) &= \int_{-\frac{2}{\cos\psi}}^{0} f_1^{\mathrm{sup}}\left(\overline{\xi}\right)\mathrm{e}^{-\mathrm{i}C\overline{\xi}\cos\psi}\mathrm{d}\overline{\xi} \\ &= -\frac{\mathrm{e}^{2\mathrm{i}C}}{\mathrm{i}C\,\cos\psi}\left\{(1+\mathrm{i})\mathrm{e}^{-2\mathrm{i}C}\sqrt{2B}\,\mathrm{ES}^*\left(2(B-C)\right) - (1+\mathrm{i})E^*\left(2B\right) + 1 - \mathrm{e}^{-2\mathrm{i}C}\right\}\end{aligned} \tag{27}$$

where ES^* is the modified Fresnel integral introduced in [32] as

$$\mathrm{ES}^*(z) = \frac{E^*(z)}{\sqrt{z}} = \frac{1-\mathrm{i}}{2}\frac{\Phi^0\left(\sqrt{\mathrm{i}z}\right)}{\sqrt{z}}.$$

In the subcritical case, defining the complex amplitude of the source distribution as

$$f_1^{\mathrm{sub}}\left(\overline{\xi}\right) = \Phi^0\left(\left[-\mathrm{i}A'_1\overline{\xi}\cos\psi\right]^{1/2}\right) - 1$$

yields the following aeroacoustic transfer function

$$\begin{aligned}\mathcal{L}_1^{\mathrm{sub}}(k'_x, k'_y) &= \int_{-\frac{2}{\cos\psi}}^{0} f_1^{\mathrm{sub}}\left(\overline{\xi}\right)\mathrm{e}^{-\mathrm{i}C\overline{\xi}\cos\psi}\mathrm{d}\overline{\xi} \\ &= -\frac{\mathrm{e}^{2\mathrm{i}C}}{\mathrm{i}C\cos\psi}\left\{(1+\mathrm{i})\sqrt{2A'_1}\mathrm{ES}^*\left(2(A'_1-C)\right)\mathrm{e}^{-2\mathrm{i}C} - \Phi^0\left(\left[2\mathrm{i}A'_1\right]^{1/2}\right) + 1 - \mathrm{e}^{-2\mathrm{i}C}\right\}.\end{aligned} \tag{28}$$

It can be noticed that both Eqs. (27) and (28) contain the term $-\mathrm{e}^{-2\mathrm{i}C}$ within the curly brackets. According to Amiet [33], the equivalent of this term for the unswept edge cancels out the contribution of the incident pressure P_0 to the sound radiation from the trailing edge. Therefore, it is omitted in the following noise calculations in order to take into account the effect of both the incident and disturbance pressures.

2.3.2. Leading-edge back-scattering aeroacoustic transfer function

The complex amplitude of the leading-edge back-scattering disturbance pressure is defined, in the supercritical case, as

$$\begin{aligned}f_2^{\mathrm{sup}}(\overline{\xi}) =& H\,\mathrm{e}^{\mathrm{i}(\alpha\overline{k}'_x + M_x\overline{\mu} - \overline{\kappa})\overline{\xi}\cos\psi} \\ &\times\left[\mathrm{i}\left\{\overline{k}'_x + M_x\overline{\mu} - \overline{\kappa}\right\}\left\{F(\overline{\xi}\cos\psi)\right\}^c + \frac{1}{\cos\psi}\left\{\frac{\partial F(\overline{\xi}\cos\psi)}{\partial\overline{\xi}}\right\}^c\right]\end{aligned} \tag{29}$$

with the parameter

$$H = \frac{(1+\mathrm{i})\mathrm{e}^{-4\mathrm{i}\overline{\kappa}}}{2\sqrt{\pi}(\alpha-1)\overline{k}_x'}\frac{1-\Theta_1^2}{\sqrt{A_1}}.$$

The corresponding aeroacoustic transfer function can be expressed as

$$\begin{aligned}\mathcal{L}_2^{\mathrm{sup}} &= \int_{-2/\cos\psi}^{0} f_2^{\mathrm{sup}}(\overline{\xi})\mathrm{e}^{-\mathrm{i}C\,\overline{\xi}\cos\psi}\mathrm{d}\overline{\xi} \\ &= \frac{H\,\mathrm{e}^{2\mathrm{i}D}}{\cos\psi}\int_0^2 \left[\mathrm{i}\left\{\overline{k}_x' + M_x\overline{\mu} - \overline{\kappa}\right\}\{F(u)\}^c + \left\{\frac{\partial F(u)}{\partial u}\right\}^c\right]\mathrm{e}^{-\mathrm{i}Du}\mathrm{d}u \end{aligned} \tag{30}$$

by means of the variable transformation $u = \overline{\xi}\cos\psi + 2$ and by defining the parameter

$$D = C - (\alpha\overline{k}_x' + M_x\overline{\mu} - \overline{\kappa}).$$

It can be noticed that, for $\psi = 0$, the expression of D corresponds to that given in [23]:

$$D(\psi = 0) = \overline{\kappa} - \overline{\mu}\frac{x_1}{S_0}.$$

The analytical solution of the integral of Eq. (30) is obtained by following the same method as in [23] for the unswept case, yielding

$$\mathcal{L}_2^{\mathrm{sup}} = \frac{H}{\cos\psi}\left(\left\{\mathrm{e}^{4\mathrm{i}\overline{\kappa}}[1-(1+\mathrm{i})E^*(4\overline{\kappa})]\right\}^c - \mathrm{e}^{2\mathrm{i}D} + \mathrm{i}[D + \overline{k}_x' + M_x\overline{\mu} - \overline{\kappa}]G\right) \tag{31}$$

with the parameter

$$\begin{aligned} G = {} & (1+\varepsilon)\mathrm{e}^{\mathrm{i}(2\overline{\kappa}+D)}\frac{\sin(D-2\overline{\kappa})}{D-2\overline{\kappa}} + (1-\varepsilon)\mathrm{e}^{\mathrm{i}(-2\overline{\kappa}+D)}\frac{\sin(D+2\overline{\kappa})}{D+2\overline{\kappa}} \\ & + \frac{(1+\varepsilon)(1-\mathrm{i})}{2(D-2\overline{\kappa})}\mathrm{e}^{\mathrm{i}4\overline{\kappa}}E^*\left[4\overline{\kappa}\right] - \frac{(1-\varepsilon)(1+\mathrm{i})}{2(D+2\overline{\kappa})}\mathrm{e}^{-\mathrm{i}4\overline{\kappa}}E\left[4\overline{\kappa}\right] \\ & + \frac{\mathrm{e}^{\mathrm{i}2D}}{\sqrt{2}}\sqrt{2\overline{\kappa}}\,\mathrm{ES}^*(2D)\left[\frac{(1-\varepsilon)(1+\mathrm{i})}{D+2\overline{\kappa}} - \frac{(1+\varepsilon)(1-\mathrm{i})}{D-2\overline{\kappa}}\right]. \end{aligned}$$

Similarly, the complex amplitude of the leading-edge disturbance pressure in the subcritical case is defined as

$$\begin{aligned} f_2^{\mathrm{sub}}(\overline{\xi}) = {} & H'\,\mathrm{e}^{\mathrm{i}(\alpha\overline{k}_x' + M_x\overline{\mu} - \mathrm{i}\overline{\kappa'})\overline{\xi}\cos\psi} \\ & \times\left[\mathrm{i}\left\{\overline{k}_x' + M_x\overline{\mu} - \mathrm{i}\overline{\kappa'}\right\}\left(F'(\overline{\xi}\cos\psi)\right) + \frac{1}{\cos\psi}\left(\frac{\partial F'(\overline{\xi}\cos\psi)}{\partial\overline{\xi}}\right)\right] \end{aligned} \tag{32}$$

with the parameter

$$H' = \frac{(1+\mathrm{i})(1-\Theta_1'^2)}{2\sqrt{\pi}(\alpha-1)\overline{k}_x'\sqrt{A_1'}}.$$

The subcritical aeroacoustic transfer function can be formulated as

$$\begin{aligned}
\mathcal{L}_2^{\mathrm{sub}} &= \int_{-2/\cos\psi}^{0} f_2^{\mathrm{sub}}(\overline{\xi})\mathrm{e}^{-\mathrm{i}C\,\overline{\xi}\cos\psi}\mathrm{d}\overline{\xi} \\
&= \frac{H'\mathrm{e}^{-2\mathrm{i}D'}}{\cos\psi}\int_0^2 \left[\mathrm{i}(\overline{k}_x' + M_x\overline{\mu} - \mathrm{i}\overline{\kappa'})\left(1-\mathrm{erf}\left(\sqrt{2\overline{\kappa'}u}\right)\right)\right. \\
&\left. +\frac{\partial}{\partial u}\left(1-\mathrm{erf}\left(\sqrt{2\overline{\kappa'}u}\right)\right)\right]\mathrm{e}^{\mathrm{i}D'u}\mathrm{d}u \\
&= \frac{H'\mathrm{e}^{-2\mathrm{i}D'}}{\cos\psi}\left\{\left(1-\mathrm{erf}\left(\sqrt{4\overline{\kappa'}}\right)\right)\mathrm{e}^{2\mathrm{i}D'} - 1\right. \\
&\left. +\mathrm{i}(\mathrm{A}' - \mathrm{D}')\int_0^2 \left(1-\mathrm{erf}\left(\sqrt{2\overline{\kappa'}\mathrm{u}}\right)\right)\mathrm{e}^{\mathrm{i}\mathrm{D}'\mathrm{u}}\mathrm{du}\right\}. \qquad (33)
\end{aligned}$$

with the parameter

$$D' = \alpha\overline{k}_x' + M_x\overline{\mu} - \mathrm{i}\overline{\kappa'} - C.$$

Again, for $\psi = 0$, the parameter D' corresponds to the original unswept formulation [23]:

$$D'(\psi = 0) = \overline{\mu}\frac{x_1}{S_0} - \mathrm{i}\overline{\kappa'}.$$

The last remaining integral of Eq. (33) can be solved as follows:

$$\begin{aligned}
&\int_0^2 \left(1-\mathrm{erf}\left(\sqrt{2\overline{\kappa'}u}\right)\right)\mathrm{e}^{\mathrm{i}D'u}\mathrm{d}u = \left(1-\mathrm{erf}\left(\sqrt{4\overline{\kappa'}}\right)\right)\frac{\mathrm{e}^{2\mathrm{i}D'}}{\mathrm{i}D'} \\
&-\frac{1}{\mathrm{i}D'} + \frac{2\sqrt{2\overline{\kappa'}}}{\mathrm{i}D'}\mathrm{ES}^*(-2\,D'^*). \qquad (34)
\end{aligned}$$

Therefore, the subcritical leading-edge aeroacoustic transfer function is

$$\begin{aligned}
\mathcal{L}_2^{\mathrm{sub}} &= \frac{H'\mathrm{e}^{-2\mathrm{i}D'}}{D'\cos\psi}\left\{A'\left[\left(1-\mathrm{erf}\left(\sqrt{4\overline{\kappa'}}\right)\right)\mathrm{e}^{2\mathrm{i}D'} - 1\right]\right. \\
&\left. +2\sqrt{2\overline{\kappa'}}(A' - D')\mathrm{ES}^*(-2D'^*)\right\}. \qquad (35)
\end{aligned}$$

Finally, for $\psi = 0$,

$$A' - D' = \overline{K} + \overline{\mu}\left(M_0 - \frac{x_1}{S_0}\right),$$

consistent with the unswept formulation.

2.4. Far-field sound power spectral density

As pointed out by Amiet in [22], the wall pressure measured at a given point and frequency, ω, is made up of many spectral components of the form $p = p_0\mathrm{e}^{\mathrm{i}[\omega(t-x/U_c)-k_y y]}$. The convective wavenumber, K_c, and the convective speed, U_c, are variable, but their product $K_c\,U_c = \omega$ is constant. Consequently, the sound power spectral density (PSD) at a given frequency results from the

summation of the contributions of all these spectral components. A simplification is introduced at this point, considering that a frequency ω is associated with a single value of U_c. For an unswept airfoil, this also determines a unique value of K_c. This is consistent with Taylor's hypothesis [34] of frozen convection of the aerodynamic field generating the wall-pressure fluctuations. However, the convective speed, U_c, is not aligned with the frame of reference attached to the trailing edge of the swept airfoil represented in Fig. 1. Therefore the dispersion relation becomes

$$\omega = \mathbf{U}_c \cdot \mathbf{K} = K'_c \, U_c \cos\psi + k'_y \, U_c \sin\psi. \tag{36}$$

Consequently, for given ω and U_c, the sound PSD is given by the contribution of all the gusts the wavenumbers of which (K'_c, k'_y) satisfy the following equation:

$$K'_c = \frac{\omega}{U_c \cos\psi} - k'_y \tan\psi. \tag{37}$$

Equation (37) states that, in the swept-airfoil case, there is no longer a unique chordwise wavenumber K'_c associated with the frequency ω, but rather a set of values depending on k'_y.

Equation (26) expresses the far-field acoustic pressure at a given frequency and observer position due to a single disturbance pressure gust. Following the argumentation of Amiet [15, p. 409-410] and Roger & Moreau [23, p. 499-500], it can be shown that the acoustic PSD due to all incident gusts contributing to the frequency ω is

$$\begin{aligned} S_{pp}(\mathbf{x},\omega) &= \left(\frac{\omega \, x_3 \, \cos\psi \, Lb}{2\pi \, c_0 \, S_0^2}\right)^2 \\ &\times \frac{1}{b} \int_{-\infty}^{+\infty} \Pi_0\left(\omega, \overline{k}'_y\right) \operatorname{sinc}^2\left\{\frac{L}{2b}\left[\overline{k}'_y - \frac{\overline{k}}{\beta_0^2}\left(\frac{\beta_x^2 x_2}{S_0} - M_y\right)\right]\right\} \left|\mathcal{L}\left(\overline{K}'_c, \overline{k}'_y\right)\right|^2 \mathrm{d}\overline{k}'_y \end{aligned} \tag{38}$$

where $\Pi_0(\omega, k'_y)$ denotes the wavenumber spectral density of incident wall-pressure fluctuations. The expression of the PSD is equal for both angular frequencies $\pm\omega$; it must be doubled to be compared with measured PSD.

A sine cardinal squared function appears within the integral of Eq. (38). The asymptotic limit for aspect ratio, $L/2b$, tending to infinity of the sine cardinal squared is a Dirac delta function:

$$\begin{aligned} &\lim_{L/2b\to+\infty} \operatorname{sinc}^2\left(\frac{L}{2b}\left[\overline{k}'_y - \frac{\overline{k}}{\beta_0^2}\left(\frac{\beta_x^2 x_2}{S_0} - M_y\right)\right]\right) \\ &= \frac{2\pi b}{L}\delta\left(\overline{k}'_y - \frac{\overline{k}}{\beta_0^2}\left(\frac{\beta_x^2 x_2}{S_0} - M_y\right)\right). \end{aligned} \tag{39}$$

Equation (38) can be simplified by substituting Eq. (39) in the integral, resulting in the asymptotic formulation

$$S_{pp}^{\infty}(\mathbf{x},\omega) = \left(\frac{\omega \, x_3 \, \cos\psi \, b}{c_0 \, S_0^2}\right)^2 \frac{L}{2\pi} \, \Pi_0\left(\omega, \overline{K}'_y\right) \left|\mathcal{L}\left(\overline{K}'_c, \overline{K}'_y\right)\right|^2 \tag{40}$$

with

$$\overline{K}'_y = \frac{\overline{k}}{\beta_0^2}\left(\frac{\beta_x^2 x_2}{S_0} - M_y\right). \tag{41}$$

The effect of this large-span simplification is to select a privileged oblique gust for the computation of the sound PSD at a given x_2 coordinate. In this case, the observer hears only that gust which produces an acoustic wavefront normal to the line joining airfoil and observer [15]. Parametric tests presented by Moreau & Roger [24] show that an aspect ratio $L/2b = 3$ is enough to ensure good results in the mid-span plane using the asymptotic formula given by Eq. (41). In summary, when the asymptotic formulation is used, the unique skewed gust contributing to the sound radiated at a given frequency, ω, and observer position, $\mathbf{x}$, is determined by Eqs. (37) and (41). It can also be noticed that the squared cosine of the sweep angle appears at the numerator of the general expression of the sound PSD: the same conclusion was reached by Ffowcs Williams and Hall [35] by different means.

Regardless of the selected model of wall-pressure statistics, which will be discussed in the next section, the aeroacoustic transfer functions presented in this section allow for an evaluation of how the sweep angle modifies the directivity patterns of the noise emitted by the interaction of the trailing edge with a given three-dimensional incident pressure gust. A parametric study of the directivity is presented in Fig. 2. The first test case concerns an incident gust with $k_y = 0$, i.e. a parallel gust in the frame of reference of an unswept airfoil. It can be seen in Figs. 2(a), 2(b), that the directivity of the sound emitted by an unswept airfoil due to a parallel incident pressure gust is symmetric with respect to the plane normal to the wall with $x_2 = 0$. However, the same gust convected past the trailing edge of an airfoil with $\psi = 15^o$ produces a non-symmetric sound directivity pattern. This effect is only slightly visible in the compact regime (Fig. 2(a)), but prominent in the non-compact regime (Fig. 2(b)). It is interesting to compare qualitatively the effect of sweep with that of the gust skewness. To do so, we define the oblique angle, or skewness, of a gust as $\gamma = \arctan(k_y/k_x)$. The directivity of sound emitted by an unswept airfoil due to two impinging gusts, one parallel ($\gamma = 0$) and one skewed ($\gamma = 15^o$), is represented in Figs. 2(c), 2(d). Whereas in the compact regime (Fig. 2(c)) the skewed gust produces a directivity nearly aligned with the axis pointing normal to the plane of the figure, in the non-compact regime (Fig. 2(d)) the directivity is very similar to that of Fig. 2(b). This is a direct consequence of Eq. (3). Finally, the combined effect of sweep and gust skewness is assessed in Figs. 2(e), 2(f), where the airfoil has $\psi = 15^o$. As already pointed out, the difference between directivity patterns is more apparent in the non-compact regime (Fig. 2(f)). In this case, the gust with $\gamma = 0$ behaves as a skewed gust due to sweep, as seen in the first test case. Interestingly, the gust having $\gamma = -15^o$ generates an almost symmetric sound directivity, due to the compensation between opposite sweep and skewness effects. However, the directivity pattern is not perfectly symmetric due to the inherent asymmetry of the underlying surface.

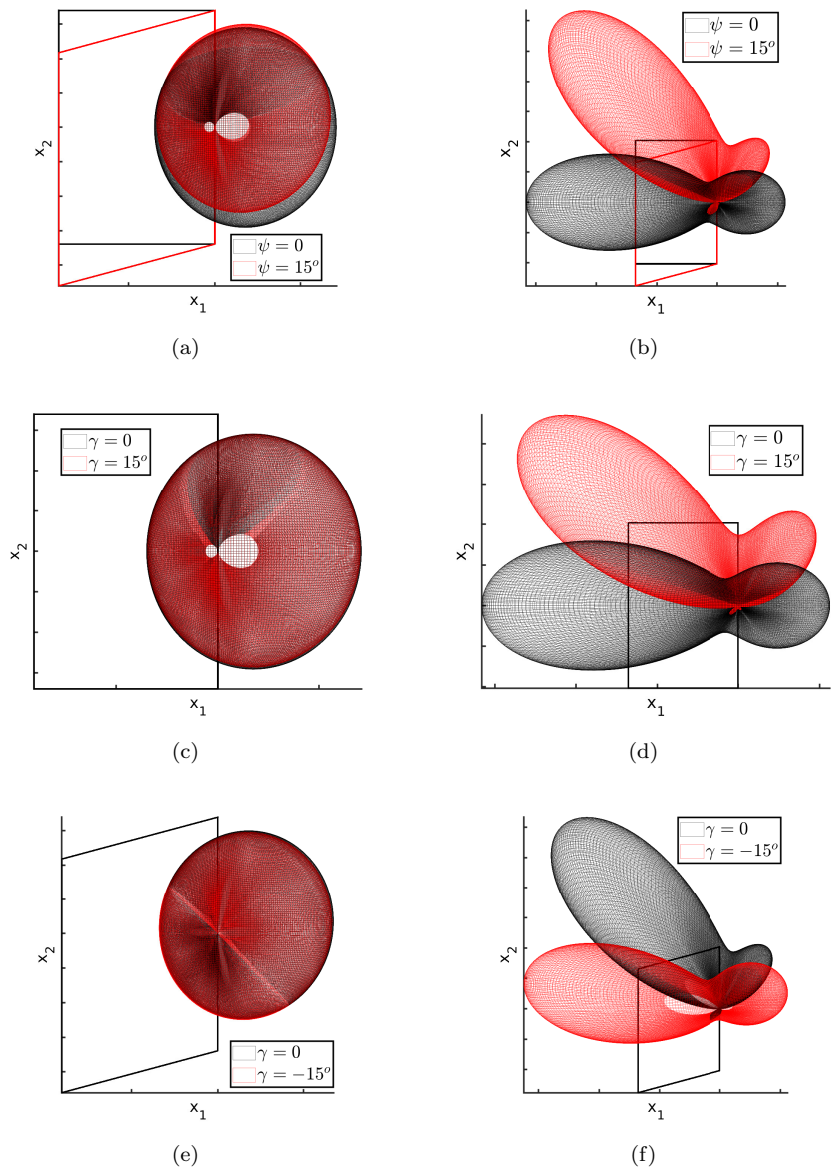

Figure 2: Study of the effect of sweep and of gust skewness on acoustic power directivity in the compact and non-compact regime. Left column: $kc = 0.25$. Right column: $kc = 5$. Observer on a half-sphere seen from above (upper x_3 axis), arbitrary units. $M_0 = 0.47$, aspect ratio $L/c = 1.5$. (a) $\gamma = 0$. (b) $\gamma = 0$. (c) $\psi = 0$. (d) $\psi = 0$. (e) $\psi = 15^o$. (f) $\psi = 15^o$.

3. Wavenumber-frequency spectral density of wall-pressure fluctuations

3.1. Original Corcos' model

The closure of Eqs. (38) and (40) is obtained by defining the PSD of the incident wall-pressure fluctuations at frequency ω and spanwise wavenumber k_y. This derives from the complete frequency-wavenumber wall-pressure PSD, defined as

$$\Pi\left(k_x, k_y, \omega\right) = \frac{1}{4\pi^2} \iint_{-\infty}^{+\infty} \Gamma_{pp}(\eta_x, \eta_y, \omega)\, \mathrm{e}^{\mathrm{i}(k_x \eta_x + k_y \eta_y)}\, \mathrm{d}\eta_x \mathrm{d}\eta_y \tag{42}$$

where $\Gamma(\eta_x, \eta_y, \omega)$ is the space-frequency cross-spectral density. The quantity of interest is then the integral of Eq. (42) with respect to k_x:

$$\Pi_0\left(\omega, k_y\right) = \int_{-\infty}^{+\infty} \Pi\left(k_x, k_y, \omega\right) \mathrm{d}k_x. \tag{43}$$

It can also be noticed that the single-point wall-pressure frequency spectrum is the integral of Eq. (42) over both wavenumbers:

$$\varphi_{pp}(\omega) = \iint_{-\infty}^{+\infty} \Pi\left(k_x, k_y, \omega\right) \mathrm{d}k_x \mathrm{d}k_y. \tag{44}$$

The complete frequency-wavenumber PSD, $\Pi\left(k_x, k_y, \omega\right)$, could be provided by Direct Numerical Simulation, for instance, but for preliminary acoustic evaluation, empirical or semi-analytic models are often used. A model of the wall-pressure statistics widely applied in literature is Corcos' [36]. Since this model can illustrate the effect of sweep on the wall-pressure statistics and then on the predicted acoustic pressure, its main features are hereby described, assuming a frame of reference (x, y) where the convection speed of wall-pressure fluctuations is aligned with the axis x, representative of an unswept airfoil. The effect of sweep will be introduced at a later stage.

The first hypothesis of Corcos' model is that the space-frequency cross-spectral density can be expressed as the product of simpler functions of separated spatial variables:

$$\Gamma_{pp}(\eta_x, \eta_y, \omega) = \varphi_{pp}(\omega)\, A(\eta_x, \omega)\, B(\eta_y, \omega)\, \mathrm{e}^{-\mathrm{i}\, K_c\, \eta_x} \tag{45}$$

where $A(\eta_x, \omega)$ and $B(\eta_y, \omega)$ are the real-valued longitudinal and lateral coherence functions, respectively. The phase shift is given by $K_c\, \eta_x$, assuming that the x axis is aligned with the convective speed of wall-pressure fluctuations. The substitution of Eq. (45) in Eq. (42) yields

$$\begin{aligned} \Pi\left(k_x, k_y, \omega\right) = \varphi_{pp}(\omega)\, \frac{1}{2\pi} \int_{-\infty}^{+\infty} A(\eta_x, \omega) \mathrm{e}^{\mathrm{i}(k_x - K_c)\eta_x}\, \mathrm{d}\eta_x \\ \times \frac{1}{2\pi} \int_{-\infty}^{+\infty} B(\eta_y, \omega) \mathrm{e}^{\mathrm{i}k_y \eta_y}\, \mathrm{d}\eta_y. \end{aligned} \tag{46}$$

The longitudinal and lateral correlations can be defined as

$$A(\eta_x,\omega)=\frac{|\Gamma(\eta_x,0,\omega)|}{\varphi_{pp}(\omega)},\qquad\qquad B(\eta_y,\omega)=\frac{|\Gamma(0,\eta_y,\omega)|}{\varphi_{pp}(\omega)},\tag{47}$$

without making any further assumption on the shape of these functions. The substitution of Eqs. (47) and (46) in Eq. (43) shows that the longitudinal coherence function has no effect on the calculation of $\Pi_0(\omega,k_y)$, at least within the hypothesis of zero sweep. In fact,

$$\begin{aligned}&\frac{1}{2\pi}\iint_{-\infty}^{+\infty}A(\eta_x,\omega)\mathrm{e}^{\mathrm{i}(k_x-K_c)\eta_x}\,\mathrm{d}\eta_x\mathrm{d}k_x\\&=\frac{1}{2\pi}\iint_{-\infty}^{+\infty}\frac{|\Gamma(\eta_x,0,\omega)|}{\varphi_{pp}(\omega)}\mathrm{e}^{\mathrm{i}(k_x-K_c)\eta_x}\,\mathrm{d}\eta_x\mathrm{d}k_x\\&=\int_{-\infty}^{+\infty}\frac{\Pi(k_x^*,\omega)}{\varphi_{pp}(\omega)}\mathrm{d}k_x^*=\frac{\varphi_{pp}(\omega)}{\varphi_{pp}(\omega)}=1\quad\text{with }k_x^*=k_x-K_c.\end{aligned}$$

Therefore, only the lateral correlation function determines the value of $\Pi_0(\omega,k_y)$. This is consistent with the physics of span-wise distributed sources concentrated at the trailing edge of the airfoil, as pointed out in [23, 37]. Furthermore, defining the lateral correlation length of wall-pressure fluctuations as

$$l_y(\omega,k_y)=\int_0^{\infty}B(\eta_y,\omega)\mathrm{e}^{\mathrm{i}k_y\eta_y}\,\mathrm{d}\eta_y,\tag{48}$$

we can express the wall-pressure PSD as

$$\Pi_0\left(\omega,k_y\right)=\frac{1}{\pi}\,\varphi_{pp}(\omega)\,l_y(\omega,k_y),\tag{49}$$

consistently with the formulation used by [23].

The second hypothesis of Corcos' model concerns the expressions of the coherence functions, which are assumed to be exponentials:

$$A(\eta_x,\omega)=\mathrm{e}^{-|\eta_x|\,\alpha_\omega}\qquad\qquad B(\eta_y,\omega)=\mathrm{e}^{-|\eta_y|\,\beta_\omega}\tag{50}$$

with $\alpha_\omega=\alpha_x\omega/U_c$ and $\beta_\omega=\alpha_y\omega/U_c$. In the following calculations, the constants $\alpha_x=0.10$ and $\alpha_y=0.77$ will be used, which are within the typical range for smooth rigid walls (see [38]). The substitution of Eqs. (50) in Eq. (46) yields Corcos' frequency-wavenumber PSD of wall-pressure fluctuations:

$$\Pi(k_x,k_y,\omega)=\varphi_{pp}(\omega)\,\frac{\frac{1}{\pi\,\alpha_\omega}}{1+\left(\frac{k_x-K_c}{\alpha_\omega}\right)^2}\,\frac{\frac{1}{\pi\,\beta_\omega}}{1+\left(\frac{k_y}{\beta_\omega}\right)^2}.\tag{51}$$

Finally, substituting Eq. (51) in Eq. (43) and comparing the result with Eq. (49), it can easily be shown that

$$l_y(\omega,k_y)=\frac{\beta_\omega}{\beta_\omega^2+k_y^2}.\tag{52}$$

3.2. Generalised Corcos' model

Corcos' model owes its popularity to the mathematical advantages outlined in the previous paragraph, namely the decoupling of the space/wavenumber variables and the capability to go easily from the space/time to the wavenumber/frequency domain. However, this model is also known to overestimate the contribution of the subconvective k_x range to a given reduced frequency, ω, by as much as 20 dB. A generalisation of Corcos' model that corrects the low-wavenumber behavior while preserving the mathematical advantages has been proposed by Caiazzo *et al.* [38]. This generalised model relies on the fact that the wavenumber energy distribution of Corcos' model, given in Eq. (51), is equivalent to a Lorentzian function in each wavenumber. A Lorentzian function, in turns, corresponds to the squared magnitude of a Butterworth filter of order one. Therefore, the generalised Corcos' model represents the wavenumber energy distribution with Butterworth filters of arbitrary integer orders m and n in the lateral and longitudinal directions, respectively:

$$\Pi(k_x, k_y, \omega) = \varphi_{pp}(\omega) \frac{\frac{n \sin(\pi/2n)}{\pi\, \alpha_\omega}}{1 + \left(\frac{k_x - K_c}{\alpha_\omega}\right)^{2n}} \frac{\frac{m \sin(\pi/2m)}{\pi\, \beta_\omega}}{1 + \left(\frac{k_y}{\beta_\omega}\right)^{2m}}. \tag{53}$$

It can be noticed that, consistently with the first hypothesis of Corcos' model, the order of the longitudinal filter, n, does not influence the value of $\Pi_0(\omega, k_y)$. In fact,

$$\int_{-\infty}^{\infty} \frac{\frac{n \sin(\pi/2n)}{\pi\, \alpha_\omega}}{1 + \left(\frac{k_x - K_c}{\alpha_\omega}\right)^{2n}} \mathrm{d}k_x = 1 \qquad \forall n \in \mathbb{N}. \tag{54}$$

The parameters m and n can be varied independently to obtain the desired wavenumber distribution of wall-pressure fluctuations. It was found in [38] that increasing the order of the chordwise wavenumber filter, n, brings the spectral density level closer to experimental evidence in the subconvective range. Yet, the generalised model does not overcome the main limitation of the original one. As Singer [39] pointed out, the separation of space/wavenumber variables prevents from representing correctly the wall-pressure correlation in directions that are neither parallel nor normal to the mean flow. This generalised model, however, is retained in this work because it allows assessing the effect of different $\Pi(k_x, k_y)$ distributions on the emitted noise by simply varying m and n. Also, the rotation of the wavenumber plane expressed in Eq. (3) can be readily introduced in Eq. (53) obtaining

$$\Pi(k'_x, k'_y, \omega) = \varphi_{pp}(\omega) \frac{\frac{n \sin(\pi/2n)}{\pi\, \alpha_\omega}}{1 + \left(\frac{k'_x \cos\psi + k'_y \sin\psi - K_c}{\alpha_\omega}\right)^{2n}} \frac{\frac{m \sin(\pi/2m)}{\pi\, \beta_\omega}}{1 + \left(\frac{-k'_x \sin\psi + k'_y \cos\psi}{\beta_\omega}\right)^{2m}}. \tag{55}$$

It can be noticed that the introduction of sweep generates a coupling between the longitudinal and lateral wall-pressure statistics. Since the rotated spanwise wavenumber k'_y now appears inside the longitudinal filter as well, the order n

of this filter influences the value of $\Pi_0(\omega, k'_y)$. The integration of Eq. (55) with respect to k'_x, necessary to obtain $l_y(\omega, k'_y)$ according to Eqs. (43) and (49), is not as straightforward as in the unswept case. Analytical integration is still possible but rather cumbersome, especially with increasing values of m and n. For this reason, analytical formulations of l_y for various combinations of m and n have been obtained by means of the open-source symbolic computation language SageMath-8.2.

3.3. Single-point wall-pressure PSD

Finally, Rozenberg's model [40] of the single-point wall-pressure PSD, $\varphi_{pp}(\omega)$, is selected for the closure of Eq. (55). This is an empirical model that takes into account the effects of Reynolds number and adverse pressure gradient, validated on a range of pipe flow and airfoil applications. The functional expression is

$$\frac{\varphi_{pp}(\omega)\, U_0}{\tau_{\max}^2 \delta^*} = \frac{\left[2.82\,\Delta^2 (6.13\,\Delta^{-0.75} + F_1)^{A1}\right]\left[4.2\left(\frac{\Pi}{\Delta}+1\right)\right]\tilde{\omega}^2}{\left[4.76\,\tilde{\omega}^{0.75} + F_1\right]^{A1} + \left[C'_3\tilde{\omega}\right]^{A2}} \tag{56}$$

with $\tilde{\omega} = \omega\,\delta^*/U_0$, $A_1 = 3.7 + 1.5\beta_C$, $A_2 = \min(3, 19/\sqrt{R_T}) + 4$, $C'_3 = 8.8\,R_T^{-0.57}$ and

$$F_1 = 4.76\left(\frac{1.4}{\Delta}\right)^{0.75}\left[0.375\,A_1 - 1\right].$$

Note that the typographical error in the definition of A_2 in [40] has been corrected.

4. Application of the swept trailing-edge theory to the computation of wall-pressure statistics and sound emission

4.1. Application case: controlled-diffusion airfoil

The numerical tests presented in this section refer to an application case analyzed in [40]: a controlled-diffusion airfoil of chord $c = 0.1356$ m with a strongly adverse pressure gradient. Reference measurements have been performed in the anechoic room of ECL by Moreau & Roger [41] and computations have been performed by Christophe *et al.* [42] for instance. The wall-pressure spectrum and the boundary-layer parameters needed for the application of Eq. (56) are collected at a location on the suction side, close to the trailing edge, where the flow is about to separate. The data, presented in Tab. 1 of [40], are $U_0 = 16.9$ m/s, $\Delta = 2.23$, $\tau_{\max} = 0.167$ Pa, $\beta_C = 20.9$, $\Pi = 8.18$ and $\alpha = 1.43$. This application case is used to test the effect of the introduction of sweep on the description of the wall-pressure statistics and on the corresponding trailing-edge sound level and directivity.

4.2. Effect of sweep angle on the wavenumber spectral density of wall-pressure fluctuations

Examples of wavenumber spectral density prescribed by Eq. (55), normalized by φ_{pp}, are depicted in Fig. 3. The left column represents cases in which the mean flow direction is aligned with the x' axis. It can be noticed that the local maxima for each $\overline{k}'_y$ correspond to a line of constant $\overline{k}'_x = \overline{K}_c = \omega\, b/U_c$. The increase of the order of the chordwise Butterworth filter, n, causes a much faster decay of the wavenumber spectral density along the $\overline{k}'_x$ axis. The increase of m has also the effect of flattening the spectral density around the maximum along the $\overline{k}'_y$ axis. The effect of sweep is introduced in the right column of Fig. 3 for the same (m, n) values. In this case, the line of local maxima is a function of $\overline{k}'_y$ expressed by Eq. (37). Also, the absolute maximum of the distribution corresponds to a $\overline{k}'_y \neq 0$ consistently with Eq. (55). The dashdotted lines in each plot represent the limit between subcritical and supercritical gusts according to Eq. (5). For $\psi = 0$ the angle of the supercritical range corresponds to $\mathrm{atan}(M_0/\beta_0)$, whereas for $\psi \neq 0$ it is slightly smaller, corresponding to $\mathrm{atan}(M_x/\beta_x)$. However, due to the rotation of the wavenumber plane, more energy enters the supercritical range, especially for $m > 1$. These considerations are consistent with those presented by Roger *et al.* [19] concerning the wavenumber energy distribution of the vortices impinging on the leading edge of a swept airfoil.

The information needed for noise prediction is the integral of the distributions depicted in Fig. 3 with respect to k'_x. This corresponds to the spanwise correlation length of wall-pressure fluctuations, l_y, according to Eq. (43). It is evident from Eq. (53) that the value of this integral is independent of n if and only if $\psi = 0$. On the contrary, the value of n is expected to play a role when $\psi \neq 0$, according to Eq. (55). Figure 4 presents the variation of the shape of l_y, obtained by analytical integration of Eq. (55), following the variation of the filter orders (m, n). Either with or without of sweep, the increase of m flattens the curve around the maximum, as already pointed out, while causing a faster decay of the correlation away from the maximum. The effect of increasing n, visible only for $\psi \neq 0$, is to increase slightly the correlation peak for a given m. However, there is only a negligible difference between the curves at $n = 2$ and $n = 3$.

4.3. Effect of sweep on far-field Sound Pressure Level and directivity

The effect of sweep on far-field Sound Pressure Level (SPL) is evaluated in Fig. 5 using the original Corcos' model (i.e. $m = 1,\ n = 1$ in Eq. (55)). The effect of the variation of the filter orders will be evaluated in the next section. The left-hand-side plot depicts the wall-pressure spectrum, $\varphi_{pp}(\omega)$, computed with Rozenberg's formulation of Eq. (56) (which agrees very well with the measurements as shown in Fig. 17(e) of [40]). The right-hand-side plot of Fig. 5 presents firstly the sound spectrum predicted for an unswept airfoil. This curve corresponds to the one depicted in Fig. 18 of [40], which also agrees

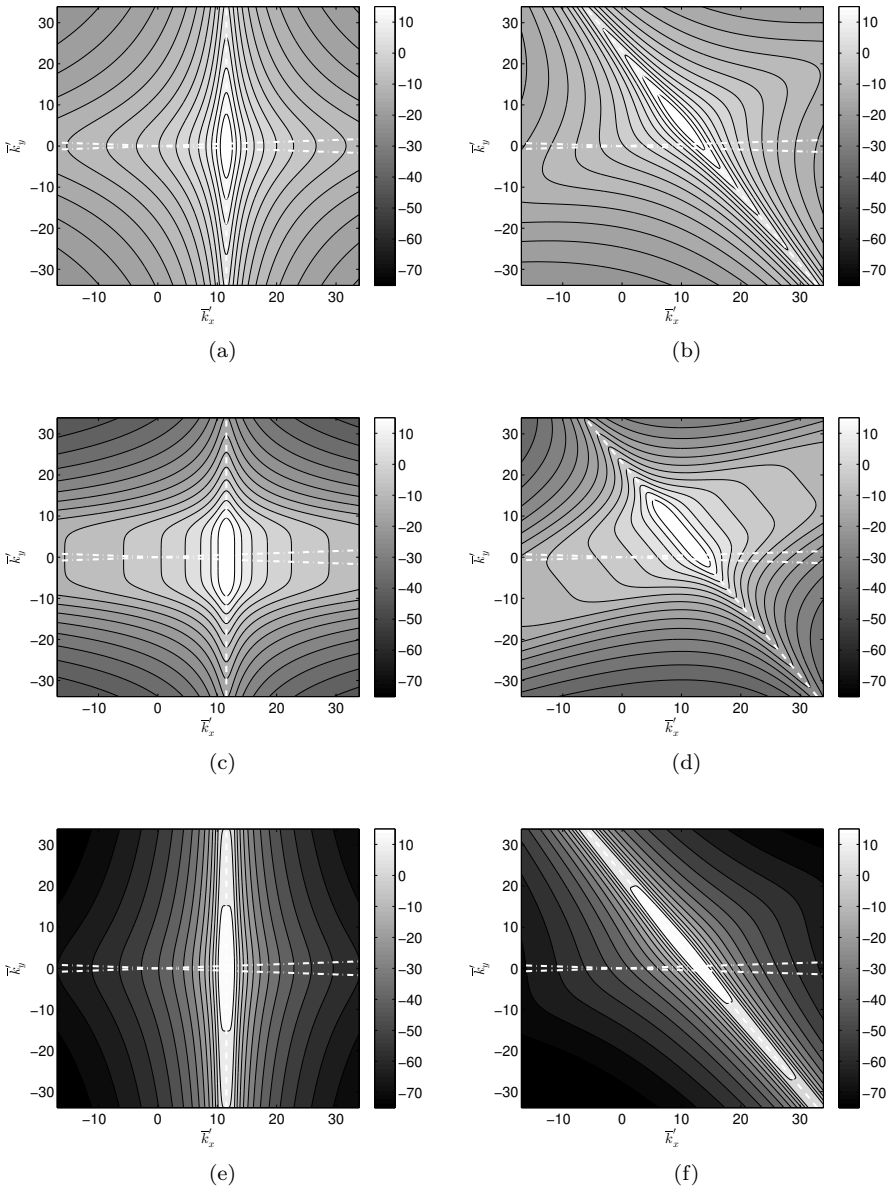

Figure 3: Normalized wavenumber wall-pressure spectral density at $f = 320$ Hz. Left column: $\psi = 0$. Right column: $\psi = 30°$. Dashed line: locus of local maxima corresponding to K_c'. Dash-dotted line: critical limit. (a) $m = 1,\ n = 1, \psi = 0$. (b) $m = 1,\ n = 1, \psi = 30°$. (c) $m = 3,\ n = 1, \psi = 0$. (d) $m = 3,\ n = 1, \psi = 30°$. (e) $m = 1,\ n = 3, \psi = 0$. (f) $m = 1,\ n = 3, \psi = 30°$.

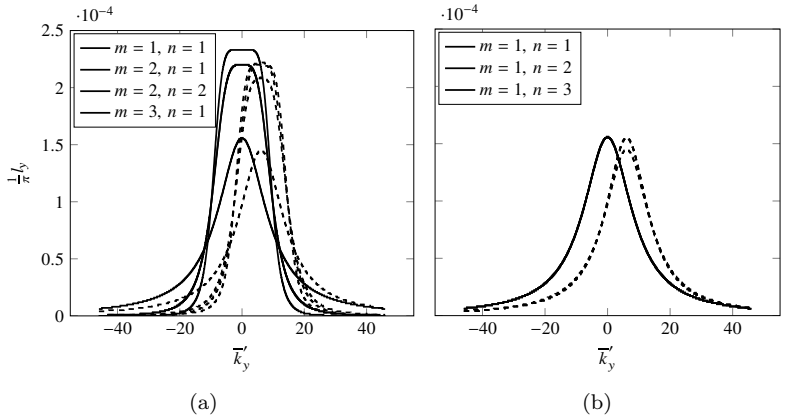

Figure 4: Spanwise correlation length of wall-pressure fluctuations at $f = 320$ Hz with various orders of the m, n filters. Plain lines: $\psi = 0°$. Dashed lines: $\psi = 30°$.

well with experimental data. It is also shown that the increase of ψ causes an overall decrease of the sound spectrum in the midspan plane.

The relative importance of the main traling-edge scattering term and of the leading-edge back-scattering correction is evaluated using the CD airfoil test case. Figure 6 shows the predicted SPL for $\psi = 0°$ and $\psi = 30°$ broken down into its main and back-scattering components. The vertical lines correspond to the reduced wavenumber $\mu = \pi/4$. As pointed out by Amiet [15], for $M \to 0$, this value limits the chord to $1/4$ of the acoustic wavelength, therefore for smaller frequencies the airfoil surface acts as a compact source of noise. It can be seen that the leading-edge correction is significant for frequencies in the compact regime, where it partially cancels the main trailing-edge contribution. This is valid for any value of the sweep angle.

Figure 7 shows the directivity of far-field noise calculated in the same test case on the upper half-sphere around the airfoil. Unlike the directivity patterns presented in Fig. 2, which are due to a single skewed gust, the ones presented in Fig. 7 are obtained with the asymptotic formulation of Eq. (39). Consequently, the radiated sound is determined by a set of skewed gusts whose k'_y wavenumbers are determined by the coordinates of the observer, x_2. At $f = 100\,\text{Hz}$ (Fig. 7(a)), the sound directivity is that of a compact dipole and the effect of sweep consists mainly in the reduction of the SPL at all observation angles. The reduction is observed at higher frequencies as well (see Figs. 7(b), 7(c)), where it is accompanied by a more prominent asymmetry of the directivity pattern.

4.4. Effect of wall-pressure wavenumber spectral distribution on Sound Pressure Level and directivity

The effect of the order of the Butterworth filters of the generalised Corcos' model is investigated in Figs. 8 and 9. Figure 8 shows that, in the midspan plane, the main effect is that of the parameter m, which can raise the SPL

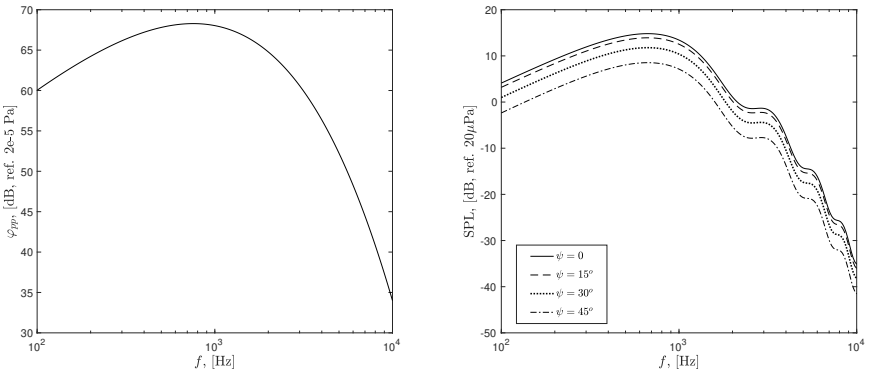

(a) (b)

Figure 5: (a) wall-pressure PSD calculated with Rozenberg's model. (b) effect of sweep on the SPL in the midspan plane ($x_1 = 0$, $x_2 = 0$) at a distance $R = 2$ m from the trailing edge.

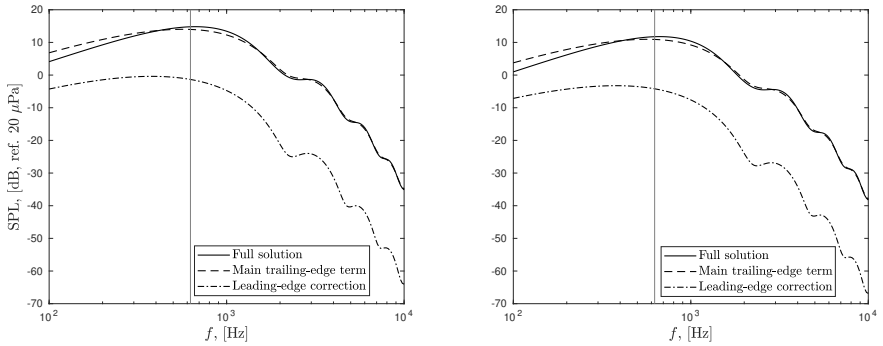

(a) (b)

Figure 6: Relative importance of the main trailing-edge scattering and leading-edge backscattering terms in the midspan plane ($x_1 = 0$, $x_2 = 0$). Vertical lines correspond to the reduced wavenumber $\mu = \pi/4$. (a) $\psi = 0°$. (b) $\psi = 30°$.

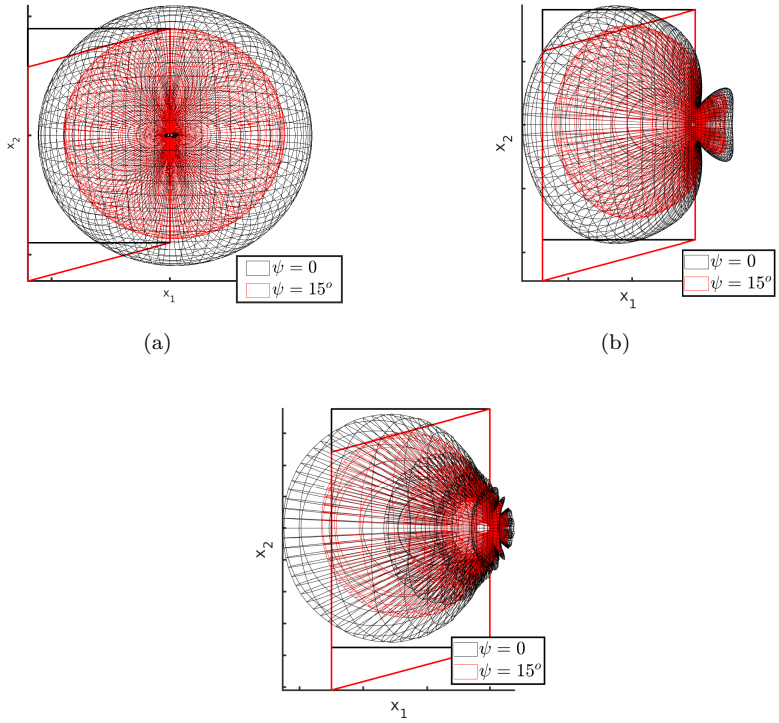

Figure 7: Effect of sweep on the predicted directivity of the noise of the CD airfoil on a half-sphere seen from above (upper x_3 axis). (a) $f = 100$ Hz. (b) $f = 2.5$ kHz. (c) $f = 10$ kHz.

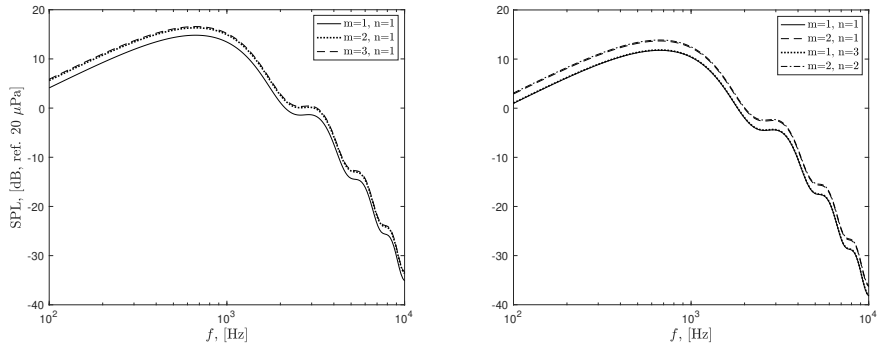

(a) (b)

Figure 8: Effect of the orders of the Butterworth filters on the SPL in the midspan plane ($x_2 = 0$) at a distance $R = 2$ m from the trailing edge. (a) $\psi = 0°$. (b) $\psi = 30°$.

spectrum by approximately 3 dB increasing from 1 to 2, as can be seen in the left-hand-side plot for $\psi = 0$. Increasing m to 3 provides only a further marginal increase of the sound PSD. For a non-zero sweep angle (Fig. 8(b)), it is possible to study the combined effect of the variations of m and n. In this case, the main effect is that of the parameter m, whereas the increase of n only provides a marginal increase of the spectral level.

The effect of the filter orders (m, n) on the directivity is shown in Fig. 9 at $f = 10$ kHz. In case the $\psi = 0$, the directivity pattern is not qualitatively changed by the increase of m, but the amplitude of the radiated sound pressure increases at all angles of observation. The directivity patterns for the $\psi = 30°$ cases confirm the observations made for the spectrum in the mid-span plane, normal to the airfoil surface. The main effect is again that of the parameter m. However, a smaller increase of the SPL at $m = 1$ can be observed for n increasing from 1 to 2.

It has been shown that the variation of the transverse correlation length of wall-pressure fluctuations, l_y, within the hypothesis of the generalised Corcos' model has a limited impact on the sound emission, quantifiable in a range of 3 dB for m varying between 1 and 3. This effect, however, might explain small discrepancies between measured and modelled spectra.

5. Connection with the strip theory for rotating blades

The reference frame considered in previous sections has axes normal and parallel to the trailing edge. Sweep is addressed by considering oblique mean flow and span ends in this frame, as illustrated in Fig. 1. Its effect if assessed for the same span length, L, and chord, $2b$, defined parallel and normal to the edges, respectively, as for the rectangular, zero-sweep airfoil. With this convention, compared three-dimensional radiation properties result from changes in either

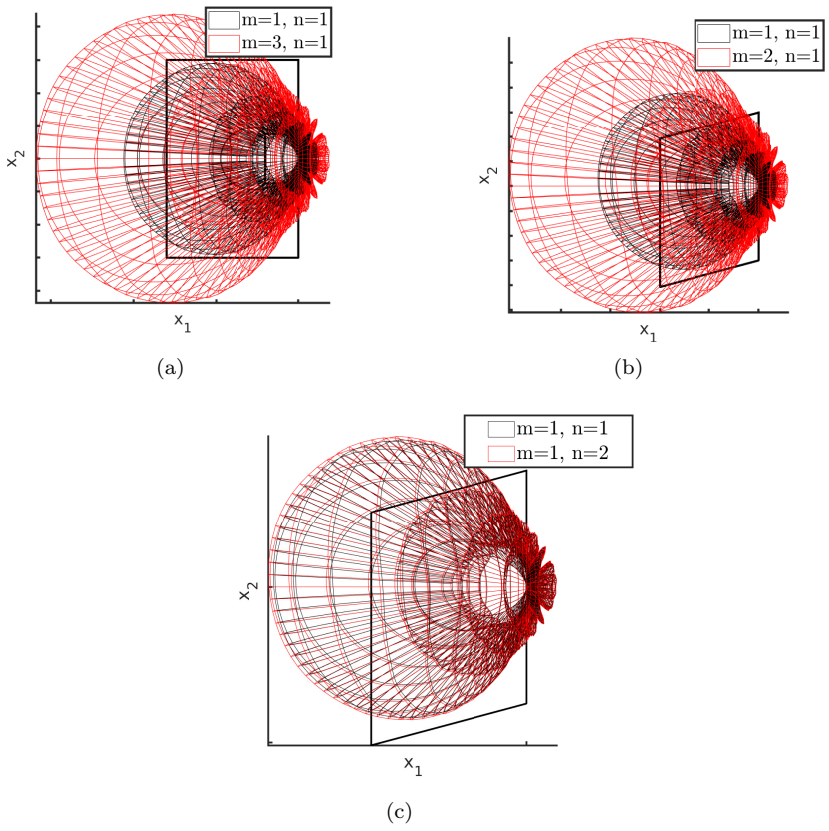

Figure 9: Effect of the order of the Butterworth filters, (m, n), on the directivity of the noise of the CD airfoil on a half-sphere seen from above (upper x_3 axis) at $f = 10$ kHz. (a) $\psi = 0$. (b) $\psi = 30°$. (c) $\psi = 30°$.

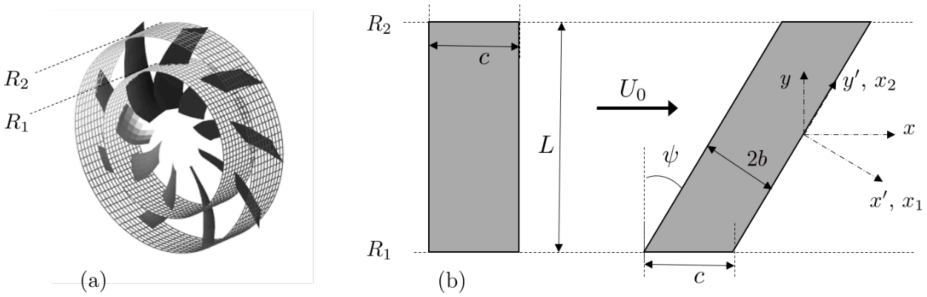

Figure 10: (a) Radial cuts of an axial-flow fan in strip theory. (b) Produced simplified flat-plate airfoil as blade segment, either straight or swept.

the sub-critical or the supercritical character of the incident wall-pressure gusts, for constant span, and to a less extent from the deformation of the rectangle into a parallelogram. Sound reduction is also expected from the reduced speed normal to the edges. A complementary point of view is provided in the present section for completeness, in connection with the strip theory usually used for axial-flow, rotating-blade noise modeling.

According to this theory, a rotor blade is split into segments limited by annular cuts. Each segment is simplified as a parallelogram airfoil. The flow is assumed free of radial velocity component, consistently with a velocity vector along the x direction, oblique in the (x_1, x_2) coordinate system. Using the alternative reference frame with axes parallel and normal to the flow direction makes sense. This is illustrated in Fig. 10 showing ideal blade segments featured by the same annular cuts on a zero-sweep blade and on a swept blade. Unlike in Fig. 1, the same radial extent L is kept for both, making the actual span of the swept, parallelogram airfoil larger, equal to $L/\cos\psi$. Furthermore, the chord, noted c, is now kept unchanged in the direction of the flow. In other words, the aspect ratio is increased for the swept airfoil. Assessing the effect of sweep by comparing the responses of both airfoil shapes in Fig. 10 leads to slightly different conclusions as those previously drawn.

Now, the way a swept blade is designed from a baseline straight one in practice can differ from one manufacturer to another. Indeed, for the same radial extent, the chord can be set constant along the flow direction or constant perpendicularly to the leading-or-trailing edge, leading to different options and constraints. This is why, to author's opinion, highlighting the effect of sweep with both conventions illustrated in Fig. 1 and Fig. 10 makes sense. It is also worth noting that, for both, the baseline and swept airfoils have the same area. Figure 11 compares the predicted responses of rectangular and parallelogram airfoils of same chord, c, in the direction of the flow and same extent normal to this direction. The wall-pressure statistics is assumed the same and is estimated by using Gliebe's empirical correlation [43], based on the mean flow speed and boundary layer thickness. The spanwise correlation length is calculated by means of the classical Corcos' model (accounting for sweep effects). The mean

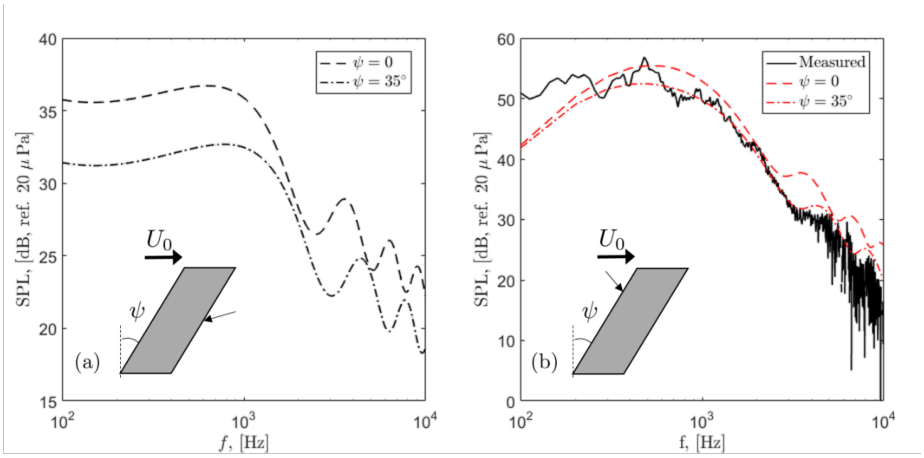

Figure 11: (a) Present trailing-edge noise predictions for the airfoil shapes shown in Fig. 10 (b) Measured turbulence-impingement noise spectrum of a swept, parallelogram airfoil of constant chord in Giez *et al* experiment, and compared predictions ignoring and accounting for sweep, reproduced from [45].

flow speed is the same as in the experiment by Giez *et al* [44] and the boundary layer thickness is set to 0.5 mm. Sound reduction is observed, as well as a significant shift of the non-compactness humps and dips towards higher frequencies. The shift can be attributed to the larger aspect ratio. Comparisons reported in Figs. 5 refer to a constant aspect ratio: the sound spectrum has some reduced level with hardly any noticeable shift of the humps and dips.

As a preliminary validation element, the trends predicted by the present trailing-edge noise model are compared with previous predictions of the turbulence-impingement (leading-edge) noise of a swept airfoil according to a similar model by Giez *et al* [44, 45]. Both models are based on the same mathematical background, namely Schwarzschild's technique applied by Amiet and its extensions. They involve a main scattering term and a secondary back-scattering term, both corresponding to half-plane problems [46]. Though the sources and the way the solution is derived are different, both models are very similar with respect to radiating properties, such as the interference effects involved in the structuring of directivity lobes, and the shifted threshold between sub-critical and supercritical gusts (pressure gusts for trailing-edge noise and velocity gusts for turbulence-impingement noise). This is especially true at subsonic Mach numbers, the flow speed having less effects than the geometry of the radiating surface. Figure 11(b) reproduces key results by Giez *et al* (both measured and predicted) for the same sweep angle of 35° as considered in Fig. 11(a). The same amount of reduction and the same qualitative dips-and-humps shift are predicted in Fig. 11(a) and Fig. 11(b). Because the predictions by Giez *et al* fit with the measured sound spectrum of the swept airfoil, the figure globally provides a first, indirect validation. Dedicated trailing-edge noise measurements

with zero-sweep and swept airfoils are well beyond the scope of the present theoretical paper. They will be the matter of future work.

6. Conclusions

The analytical developments and parametric numerical tests presented in this paper have highlighted the importance of taking into account sweep in a theory of trailing-edge noise. They provide more complete physical insight into the scattering of sound from the trailing-edge and allow assessing the potential for effective noise reduction. Furthermore, the model can be efficiently integrated in the early design stage of propellers or fans and can guide the design process to attain the target of reduced noise emissions.

The effect of sweep on generating an asymmetric directivity of far-field noise has been elucidated. Furthermore, the use of a generalised Corcos' model highlighted the fact that noise predictions can be biased by the hypothesis on the transverse correlation length of wall-pressure fluctuations. More investigation is necessary on this issue, especially in case of rotating blades where the statistics may significantly differ from the stationary airfoil case. This is all the more true since the original model of Corcos is still used for fan applications.

Acknowledgments

This paper has been published in
Journal of Sound & Vibration, **493** (2021) 115838.
doi.org/10.1016/j.jsv.2020.115838

It reports about outcomes of the project SCONE. This project has received funding from the Clean Sky 2 Joint Undertaking under the European Union's Horizon 2020 research and innovation programme under grant agreement No 755543. The Authors gratefully acknowledge the support of the Canadian NSERC Discovery Grant (no. RGPIN-2014-04111). This work was performed within the framework of the LABEX CeLyA (ANR-10-LABX- 0060) of Université de Lyon, within the program "Investissements d'Avenir" (ANR-16- IDEX-0005) operated by the French National Research Agency (ANR).

References

[1] J. Vad, Effects of sweep and spanwise changing circulation applies to airfoils: a case study, J. Appl. Comput. Mech. 5 (2).

[2] E. Envia, E. J. Kerschen, Influence of vane sweep on rotor-stator interaction noise, Tech. rep., NASA (1990).

[3] E. Envia, M. Nallasamy, Design selection and analysis of a swept and leaned stator concept, Tech. rep., NASA (1998).

[4] J. de Laborderie, S. Moreau, Prediction of tonal ducted fan noise, J. Sound Vib. 372 (2016) 105–132. doi:10.1016/j.jsv.2016.02.032.

[5] R. P. Woodward, D. M. Elliott, C. E. Hughes, J. J. Berton, Benefits of swept and leaned stators for fan noise reduction, J. Aircraft 38 (6).

[6] F. Ommi, M. Azimi, Main fan noise mitigation technologies in turbofan engines, Aviation 18 (3) (2014) 141–146. doi:10.3846/16487788.2014.969881.

[7] G. Grasso, S. Moreau, J. Christophe, C. Schram, Multi-disciplinary optimization of a contra-rotating fan, Int. J. Aeroacoust. 17 (6-8) (2018) 655–686. doi:10.1177/1475472X18789000.

[8] D. Casalino, F. Avallone, I. Gonzalez-Martino, D. Ragni, Aeroacoustic study of a wavy stator leading edge in a realistic fan/ogv stage, in: Proceedings of the International Symposium on Transport Phenomena and Dynamics of Rotating Machinery - ISROMAC, Maui, Hawaii, 2017.

[9] K. Bamberger, T. Carolus, Optimization of axial fans with highly swept blades with respect to losses and noise reduction, in: Proceedings of the FAN2012 International Conference on Fan Noise, Technology and Numerical Methods, 2012.

[10] G. Herold, F. Zenger, E. Sarradj, Influence of blade skew on axial fan component noise, Int. J. Aeroacoust. 16 (4-5) (2017) 418–430. doi:10.1177/1475472X17718740.

[11] F. Krömer, S. Becker, Experimental investigation of the off-design sound emission of low-pressure axial fans with different fan blade skew, in: Proceedings of the Euronoise 2018 Conference, Crete, 2018.

[12] F. J. Krömer, S. Moreau, S. Becker, Experimental investigation of the interplay between the sound field and the flow field in skewed low-pressure axial fans, J. Sound Vib. 442 (2019) 220 – 236. doi:https://doi.org/10.1016/j.jsv.2018.10.058.

[13] R. K. Amiet, High frequency thin-airfoil theory for subsonic flow, AIAA J. 14 (8) (1976) 1076–1082.

[14] K. Schwarzschild, Die beugung und polarisation des lichts durch einen spalt. i., Mathematische Annalen 55 (2) (1901) 177–247.

[15] R. K. Amiet, Acoustic radiation from an airfoil in a turbulent stream, J. Sound Vib. 41 (4) (1975) 407–420.

[16] Y. Rozenberg, Modélisation analytique du bruit aérodynamique à large bande des machines tournantes: utilisation de calculs moyennés de mécanique des fluides. (analytical modeling of rotating machinery aerodynamic broadband noise: use of steady-state fluid dynamic computations), Ph.D. thesis, École Centrale de Lyon, France (2007).

[17] M. Roger, A. Carazo, Blade-geometry considerations in analytical gust-airfoil interaction noise models, in: 16th AIAA/CEAS Aeroacoustics Conference (31st AIAA Aeroacoustics Conference), Stockholm, SW, 7-9 June, 2010.

[18] A. Carazo, M. Roger, M. Omais, Analytical prediction of wake-interaction noise in counter-rotation open rotors, in: Proceedings of the 17th AIAA/CEAS Aeroacoustics Conference (32nd AIAA Aeroacoustics Conference), Portland, OR, June 5 - 8, 2011.

[19] M. Roger, C. Schram, S. Moreau, On vortex–airfoil interaction noise including span-end effects, with application to open-rotor aeroacoustics, J. Sound Vib. 333 (2014) 283–306.

[20] M. E. Quaglia, T. Léonard, S. Moreau, M. Roger, A 3d analytical model for orthogonal blade-vortex interaction noise, J. Sound Vib. 399 (2017) 104–123.

[21] J. J. Adamczyk, The passage of an infinite swept airfoil through an oblique gust, Tech. rep., NASA (1974).

[22] R. K. Amiet, Noise due to turbulent flow past a trailing edge, J. Sound Vib. 4 (3) (1976) 387–393.

[23] M. Roger, S. Moreau, Back-scattering correction and further extensions of Amiet's trailing-edge noise model. Part 1: Theory, J. Sound Vib. 286 (3) (2005) 477–506.

[24] S. Moreau, M. Roger, Back-scattering correction and further extensions of amiet's trailing-edge noise model. part ii: Application, J. Sound Vib. 323 (1) (2009) 397 – 425. doi:https://doi.org/10.1016/j.jsv.2008.11.051.

[25] S. Lee, Empirical wall-pressure spectral modeling for zero and adverse pressure gradient flows, AIAA J. 56 (5) (2018) 1818–1829. doi:10.2514/1.J056528.

[26] G. Grasso, P. Jaiswal, H. Wu, S. Moreau, M. Roger, Analytical models of the wall-pressure spectrum under a turbulent boundary layer with adverse pressure gradient, J. Fluid Mech. 877 (2019) 1007–1062. doi:10.1017/jfm.2019.616.

[27] T. Nodé-Langlois, F. Wlassow, V. Languille, Y. Colin, B. Caruelle, J. Gill, X. Chen, X. Zhang, A. B. Parry, Prediction of contra-rotating open rotor broadband noise in isolated and installed configurations, in: 20th AIAA/CEAS Aeroacoustics Conference, Atlanta, GA, 16-20 June, 2014.

[28] M. Sanjosé, S. Moreau, Fast and accurate analytical modeling of broadband noise for a low-speed fan, J. Am. Soc. Acoust. 143 (3103).

[29] M. Howe, A review of the theory of trailing edge noise, J. Sound Vib. 61 (3) (1978) 437 – 465. doi:https://doi.org/10.1016/0022-460X(78)90391-7.

[30] M. Abramowitz, I. A. Stegun, Handbook of Mathematical Functions, Dover Publications, New York, 1970.

[31] N. Curle, M. J. Lighthill, The influence of solid boundaries upon aerodynamic sound, Philos. Trans. Royal Soc. London. Series A 231 (1187) (1955) 505–514. doi:10.1098/rspa.1955.0191.

[32] M. Roger, S. Moreau, Addendum to the back-scattering correction of amiet's trailing-edge noise model, J. Sound Vib. 331 (2012) 5383–5385.

[33] R. K. Amiet, Effect of the incident surface pressure field on noise due to turbulent flow past a trailing edge, J. Sound Vib. 57 (2) (1978) 305–306.

[34] G. I. Taylor, The spectrum of turbulence, Philos. Trans. Royal Soc. London. Series A 164 (919) (1938) 476 – 490.

[35] J. E. Ffowcs Williams, L. H. Hall, Aerodynamic sound generation by turbulent flow in the vicinity of a scattering half plane, J. Fluid Mech. 40 (4) (1970) 657–670.

[36] G. M. Corcos, The structure of the turbulent pressure field in boundary-layer flows, J. Fluid Mech. 18 (1964) 353–379.

[37] M. Roger, Broadband noise from lifting surfaces: Analytical modeling and experimental validation, in: R. Camussi (Ed.), Noise Sources in Turbulent Shear Flows: Fundamentals and Applications, Vol. 545 of CISM Udine Series, Springer-Verlag Wien, 2013, pp. 289–344.

[38] A. Caiazzo, R. D'Amico, W. Desmet, A generalized corcos model for modelling turbulent boundary layer wall pressure fluctuations, J. Sound Vib. 372 (2016) 192–210.

[39] B. A. Singer, Turbulent wall-pressure fluctuations: new model for off-axis cross-spectral density, Tech. rep., NASA (1996).

[40] Y. Rozenberg, G. Robert, S. Moreau, Wall-pressure spectral model including the adverse pressure gradient effects, AIAA J. 50 (10) (2012) 2168–2179.

[41] S. Moreau, M. Roger, Effect of airfoil aerodynamic loading on trailing-edge noise sources, AIAA J. 43 (1) (2005) 41–52. doi:10.2514/1.5578.

[42] J. Christophe, S. Moreau, C. W. Hamman, J. A. S. Witteveen, G. Iaccarino, Uncertainty quantification for the trailing-edge noise of a controlled-diffusion airfoil, AIAA J. 53 (1) (2015) 42–54. doi:10.2514/1.J051696.

[43] P. Gliebe, R. Mani, H. Shin, B. Mitchell, G. Ashford, S. Salamah, S. Connell, Aeroacoustic prediction codes, Tech. rep., NASA (2000).

[44] J. Giez, L. Vion, M. Roger, S. Moreau, Effect of the edge-and-tip vortex on airfoil self-noise and turbulence impingement noise, in: 22nd AIAA/CEAS Aeroacoustics Conference, 2016. doi:10.2514/6.2016-2996.

[45] S. Moreau, M. Roger, Advanced noise modeling for future propulsion systems, Int. J. Aeroacoust. 17 (6-8) (2018) 576–599. doi:10.1177/1475472X18789005.

[46] M. Roger, S. Moreau, Extensions and limitations of analytical airfoil broadband noise models, Int. J. Aeroacoust. 9 (3) (2010) 273–305. doi:10.1260/1475-472X.9.3.273.